On the sea spray aerosol originated from bubble bursting jets

Francisco J. Blanco–Rodríguez and J. M. Gordillo[†]

Área de Mecánica de Fluidos, Departamento de Ingeniería Aeroespacial y Mecánica de Fluidos, Universidad de Sevilla, Avenida de los Descubrimientos s/n 41092, Sevilla, Spain

Here we provide a theoretical framework revealing that the radius R_d of the top droplet ejected from a bursting bubble of radius R_b and $Bo \leqslant 0.05$ can be expressed as $R_d/R_b = K_b \left(1 - (Oh/Oh'_c)^{1/2} \right)$ for $Oh \lesssim Oh'_c$ or as $R_d \approx 18 \, \mu_l^2/(\rho_l \sigma)$ for $Oh \gtrsim Oh'_c$ with the numerically fitted constants $K_b \approx 0.2$, $Oh'_c \approx 0.03$, $Oh = \mu_l/\sqrt{\rho_l \, R_b \, \sigma} \ll 1$ the Ohnesorge number, $Bo = \rho_l \, g \, R_b^2/\sigma$ the Bond number, and ρ_l, μ_l and σ indicating the liquid density, dynamic viscosity and interfacial tension coefficient, respectively. These predictions, which do not only have solid theoretical roots but are also much more accurate than the usual 10% rule used in the context of marine spray generation via whitecaps for $R_b \lesssim 1$ mm, agrees very well with both experimental data and numerical simulations for the values of Oh and Bo investigated. Moreover, making use of a criterion which reveals the mechanism that controls the growth rate of capillary instabilities, we also explain here why no droplets are ejected from the tip of the fast Worthington jet for $Oh \gtrsim 0.04$. In addition, our results predict the generation of submicron-sized aerosol particles with diameters below 100 nm and velocities $\sim \sigma/\mu_l$ for bubble radii $10 \, \mu m \lesssim R_b \lesssim 20 \mu m$, within the range found in natural conditions and in good agreement with experiments, a fact suggesting that our study could be applied in the modeling of sea spray aerosol production.

1. Introduction

The breakup of ocean waves entraps air bubbles that disintegrate within the liquid bulk and burst when they rise back to the surface, ejecting into the atmosphere droplets which, after evaporation, constitute the so called sea spray aerosol (SSA), which influences climate by scattering and absorbing radiation and also because part of the solid particles composing the SSA serve as cloud condensation nuclei and ice nuclei (Veron 2015; de Leeuw *et al.* 2011; Erinin *et al.* 2019). Hence, the understanding, description and quantification of a fundamental proccess such as the bursting of bubbles at interfaces, which produce drops with different chemical compositions (Wang *et al.* 2017) depending on whether drops are formed through the disintegration of the cap film (Lhuissier & Villermaux 2012) –film drops– or via the breakup of the jet ejected upwards from the base of the collapsing cavity (MacIntyre 1972) –jet drops–, will help improve the predictive capability of climate models.

It is a common belief that most of the submicrometric particles composing SSA originate from film drops (Veron 2015) but, very recently, Wang *et al.* (2017) demonstrated that the fraction of submicrometric SSA which can be attributed to jet drops varies from 20% to 40% depending on the seawater chemical composition. The flux of SSA

from jet drops is usually calculated using, as an intermediate step, the well known 10% rule, which approximates the drop radii as $R_d = 0.1\,R_b$, with R_b the bubble radius. This approximation is commonly used and has been employed very recently in the paper by Wang *et al.* (2017). However, the numerical simulations in Duchemin *et al.* (2002) demonstrated, almost twenty years ago, that the function R_d/R_b varies non monotonically with R_b and also that $min(R_d/R_b) \sim O(0.01)$, a fact further confirmed by the more accurate numerical results reported in Brasz *et al.* (2018).

Then, motivated by its atmospheric and climate implications and by the remarkable findings in Wang *et al.* (2017), this contribution aims at improving the quantification of the SSA produced from jet drops. Here we make use of our theory in Gordillo & Rodríguez-Rodríguez (2019) and provide equations for R_d and for the initial velocity of the droplets ejected, V_d, as a function of R_b and of the physical properties of the liquid. In doing so, we will also present a new model describing the spatio-temporal evolution of the jet that, among other things, predicts the behaviour of function R_d/R_b around its minimum. Let us point out that our study is limited to the range of bubble diameters of interest for SSA production, for which gravitational effects can be neglected in a first approximation.

The paper is structured as follows: in §2 we briefly describe the numerical simulations and present some of the results obtained. Section §3 is devoted to develop a model describing the spatio-temporal evolution of the jet from its inception to its breakup and to compare our predictions with experimental and numerical results. Finally, section §4 summarizes the main results obtained.

2. Numerical setup and revision of previous results

With the main purpose of analyzing the ejection of droplets from the very fast Worthington jets ejected after the bursting of a bubble of radius R_b, here we have performed an exhaustive numerical study by varying both the Bond and Ohnesorge numbers, respectively defined as $Bo = \rho_l\,g\,R_b^2/\sigma$ and $Oh = \mu_l/\sqrt{\rho_l\,R_b\,\sigma}$, with ρ_l, μ_l and σ referring to the liquid density, dynamic viscosity and interfacial tension coefficient, respectively [see figure 1 (a)]. Here, lengths, times and pressures are made non-dimensional using as characteristic values R_b, $\sqrt{\rho_l\,R_b^3/\sigma}$ and σ/R_b and hence, velocities will be made non-dimensional using as the characteristic value the capillary velocity, $V_c = \sqrt{\sigma/(\rho_l\,R_b)}$. Dimensionless variables will be written throughout the text in lower-case letters to differentiate them from their dimensional counterparts -in capitals- and the subscript d will be used to denote quantities referring to the instant the droplet detaches from the tip of the jet.

Axisymmetric numerical simulations have been performed using the open-source code GERRIS (Popinet 2003; Deike *et al.* 2018; Brasz *et al.* 2018; Gordillo & Rodríguez-Rodríguez 2019) using as values for the density and viscosity ratios those corresponding to air bubbles in water namely, 1.2×10^{-3} and 1.8×10^{-2}. The computations are started by suddenly removing the cap of a static bubble at a free surface. The initial shape of the bubble, [see figure 1 (a)] at $T = 0$, is calculated solving the Young–Laplace equation for different values of the Bond number following the procedure detailed in Lhuissier & Villermaux (2012). Simulations with different grid refinements (maximum level of refinement varying from 10 to 14) have been carried out to check the grid independence of the results. We have further validated our numerics by comparing with Brasz *et al.* (2018) and the GERRIS script developed here is provided as part of the Supplementary Material.

Gordillo & Rodríguez-Rodríguez (2019) explained that bubble bursting jets are pro-
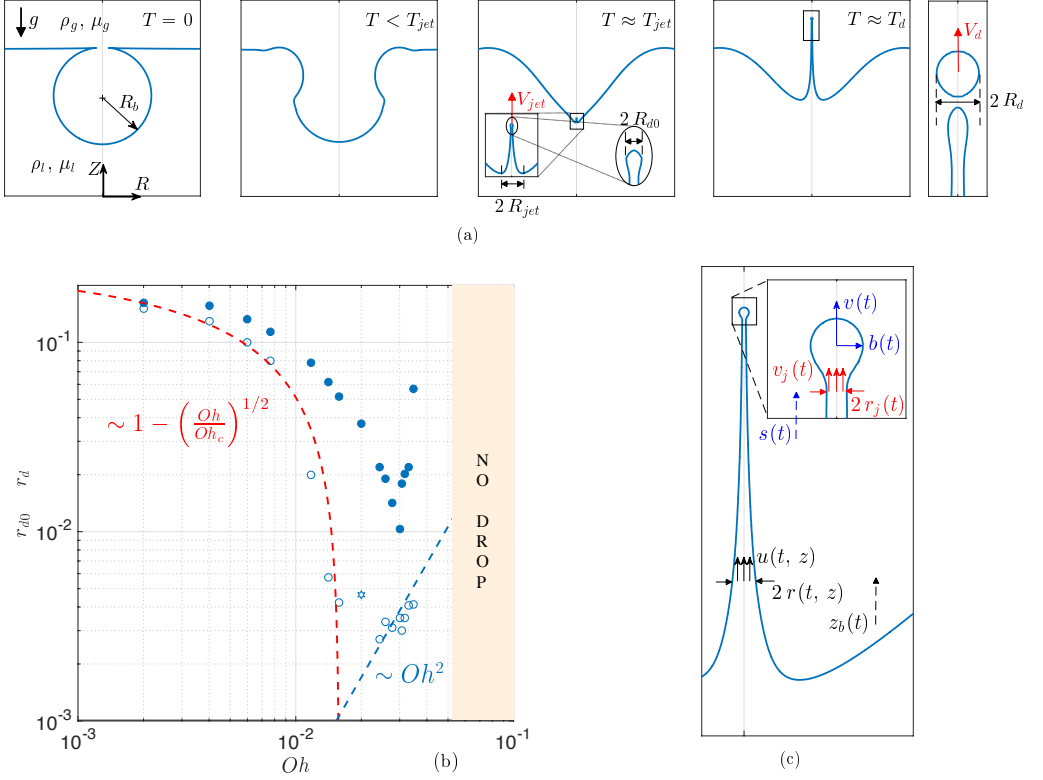
(a)

(b)

(c)

FIGURE 1. (a) Sketch showing the sequence of events following the bursting of a bubble at a free interface. The retraction of the rim causes a convergent flow towards the base of the cavity that favours the formation of a fast jet of initial velocity V_{jet} and initial radius R_{jet}. For sufficiently small values of the Ohnesorge numbers, a drop of radius R_d and velocity V_d is issued from the tip of the jet. (b) Numerical results for the dimensionless droplet radius at the ejection time (r_{d0}, open markers) and at the break-up time (r_d, filled markers) corresponding to $Bo = 0.01$ and different values of the Ohnesorge number. (c) Sketch defining the main variables used in the model developed here to predict r_d and v_d.
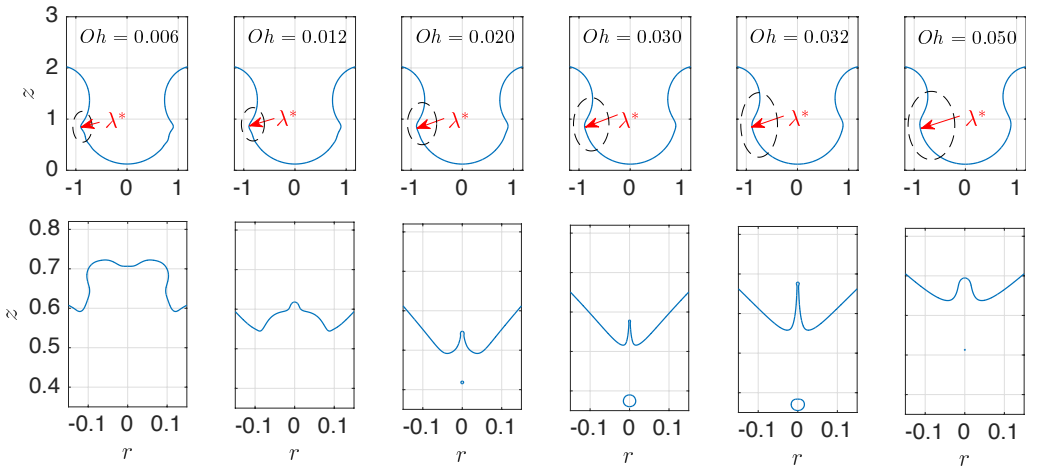

FIGURE 2. Shapes of the collapsing cavity for different values of the Ohnesorge number at two different instants of time. Observe that a tiny bubble is entrapped below the jet for $Oh_c \lesssim Oh \lesssim Oh_d$, with $Oh_c \simeq 0.02$ and $Oh_d \simeq 0.05$. Here, $Bo = 0.01$.

duced by a purely inertial mechanism in which capillarity transforms the initial spherical bubble into a truncated cone, with the radius of the base of such a cone decreasing linearly with λ^*, namely the wavelength of the capillary wave excited during the rim retraction process (see figure 2). Gordillo & Rodríguez-Rodríguez (2019) found, both theoretically and numerically, that $\lambda^* \propto Oh^{1/2}$ and also that the amplitude of this wave is $\propto \lambda^*$ for $Oh \lesssim 0.02$. Then, since the radius of the truncated cone varies linearly with λ^*, it was also predicted in Gordillo & Rodríguez-Rodríguez (2019) that the radius of the incipient jet, r_{jet} can be expressed as

$$r_{jet} \propto 1 - (Oh/Oh_c)^{1/2} \quad \text{if} \quad Oh < Oh_c(Bo) \simeq 0.02 \,, \tag{2.1}$$

with $Oh_c(Bo)$ the value of the Ohnesorge number for which the crest of the wave reaches the vertex of the cone. Notice that Oh_c depends on the Bond number because the vertex position depends on the initial shape of the static bubble, which clearly depends on the Bond number. Gordillo & Rodríguez-Rodríguez (2019) also explained that, for $Oh \lesssim Oh_c$, the initial velocity of the extremely fast and thin jet, v_{jet}, can be calculated as the flow generated by a continuous line of sinks extending upwards from the base of the truncated cone along the axis of symmetry a distance proportional to $\lambda^* \propto Oh^{1/2}$. Moreover, the intensity of these sinks also depends on $Oh^{1/2}$ through the capillary pressure, which depends on the cone geometry. All these facts explain why v_{jet} depend on $Oh^{1/2}$, with the precise functional form of v_{jet} calculated in Gordillo & Rodríguez-Rodríguez (2019) as:

$$v_{jet} \propto Oh^{1/2} \quad \text{for} \quad Oh \ll 1 \quad \text{and} \quad v_{jet} \propto \left(1 - (Oh/Oh_c)^{1/2}\right)^{-1/2} \quad \text{for} \quad Oh \approx Oh_c \,. \tag{2.2}$$

The shapes of the collapsing bubbles for different values of the Ohnesorge number is represented in figure 2 for two different instants of time. Observe that there is a remarkable difference between the two smaller values of Oh and $Oh = 0.02$: in this latter case, a tiny bubble is entrapped below the jet. This bubble is created because the crest of the capillary wave reaches the vertex of the cone for $Oh = Oh_c$ and a point below the vertex for $Oh > Oh_c$. From equation (2.2), notice that the predicted velocity would tend to infinite for $Oh = Oh_c$, but this singularity is clearly not realistic. Indeed, it was shown in Gordillo & Rodríguez-Rodríguez (2019) that, when a bubble is entrapped, the jet velocity is limited by viscous stresses and, thus, the dimensional jet velocity and jet radius are respectively given by $V_{jet} \propto \sigma/\mu_l$ and $R_{jet} \propto \mu_l^2/(\rho_l \sigma)$. These are constant values for fixed physical properties and represent the maximum achievable velocity and the minimum achievable radius (with slight deviations near $Oh = 0.03$ as it will be commented below) which, in dimensionless terms, can be expressed as

$$r_{jet} \propto Oh^2 \quad \text{and} \quad v_{jet} \propto Oh^{-1} \quad \text{for} \quad Oh > Oh_c \,. \tag{2.3}$$

The case $Oh = 0.032$ in figure 2 illustrate a case for which equations (2.3) accurately predicts the numerical results. However, for the largest value of the Ohnesorge number illustrated in figure 2, the amplitude of the capillary wave is very much attenuated by viscosity. Consequently, the crests of the capillary waves do not reach the vertex of the cone for $Oh > Oh_d$, with $Oh_d(Bo \leqslant 0.01) \simeq 0.05$. Therefore, bubbles are entrapped below the jet for values of the Ohnesorge numbers within the range

$$Oh_c(Bo) \leqslant Oh \leqslant Oh_d(Bo) \quad \text{with} \quad Oh_c(Bo \ll 1) \approx 0.02 \quad \text{and} \quad Oh_d(Bo \ll 1) \approx 0.05 \,. \tag{2.4}$$

Clearly, the predictions in equations (2.1) and (2.2) will deteriorate as Oh approaches Oh_c and, also, there will be deviations from the predictions given in equations (2.3) for

values of Oh near the boundaries limiting the bubble entrapment regime namely, Oh_c and Oh_d. In spite of this, the numerical results depicted in figure 1 (b) verify the scalings in equations (2.1) and (2.3), confirming the non-monotonic dependence of the initial radius of the jet predicted in Gordillo & Rodríguez-Rodríguez (2019). Figure 1 (b) also reveals that the radii of the ejected droplets, r_d, which is the truly important value for applications, are far larger than their initial value, r_{d0}.

Our goal in this contribution is to provide closed expressions for r_d and v_d at the instant the top droplet is emitted from the tip of the jet. For that purpose, we will derive a system of differential equations that will be integrated making use of the initial values for the jet radius and the jet velocity, which can be either calculated numerically or approximated using equations (2.1), (2.2) and (2.3). However, to do so, it will be first necessary to describe the spatio-temporal evolution of the jet width and of the jet velocity upstream the jet tip.

3. Modeling the spatio-temporal evolution of the jet

The time evolution of the jet tip velocity, $v(t)$, and of the radius of curvature of the tip of the jet, $b(t)$, can be calculated using the following mass and momentum balances (Taylor 1959),

$$\frac{ds}{dt} = v, \quad \frac{4}{3}\pi\frac{db^3}{dt} = \pi r_j^2 (v_j - v),$$
$$\frac{4}{3}\pi b^3 \frac{dv}{dt} = -\pi r_j + \pi r_j^2 (v - v_j)^2 - 6\pi Oh\left(\frac{\mu_g}{\mu_l}\right) b v, \tag{3.1}$$

with $r_j(t) = r(s(t), t)$ and $v_j(t) = u(s(t), t)$ the values of the radius $r(z, t)$ and of the vertical component of the liquid velocity $u(z, t)$ at the vertical position $z = s(t)$ where a drop of radius $b(t)$ is located [see figure 1 (c)]. In equation (3.1), notice that the dimensionless term $-\pi r_j$, results from the addition of two contributions: the interfacial tension force along the perimeter of a circle of radius r_j, $-2\pi r_j$, plus the force πr_j associated with the capillary pressure $1/r_j$ exerted on a circle of area πr_j^2. Equations (3.1) express that the jet tip is mainly decelerated by the action of interfacial tension forces, but we have also added the small force exerted by the gas because we checked that the inclusion of the Stokes drag over a sphere of radius $b(t)$, with μ_g in (3.1) the gas viscosity, slightly improves the agreement between the numerical results and the model.

Clearly, the system (3.1) can only be solved once $r_j(t)$ and $v_j(t)$ are known. For that purpose, here we make use of the ballistic equations for $r(z, t)$ and $u(z, t)$ in the form presented in Gekle & Gordillo (2010)

$$\frac{\partial r^2}{\partial t} + \frac{\partial}{\partial z}(r^2 u) = 0 \Rightarrow \frac{D}{Dt}(\ln r^2) = -S \quad \text{with} \quad S = \frac{\partial u}{\partial z} \quad \text{and}$$
$$\frac{\partial u}{\partial t} + u\frac{\partial u}{\partial z} = 0 \Rightarrow \frac{Du}{Dt} = 0, \tag{3.2}$$

with $D/Dt \equiv \partial/\partial t + u\,\partial/\partial z$ indicating the material derivative and S the strain rate.

The parabolic system of equations (3.2) can be solved using the method of characteristics in the spatio–temporal region $s(t) \geqslant z \geqslant z_b(t)$, with $z_b(t)$ the origin of the ballistic region. The solution can be found once the liquid velocity and the jet radius $u(\tau, z_b(\tau)) = u_b(\tau)$ and $r(\tau, z_b(\tau)) = r_b(\tau)$ are known functions of time at the spatio-temporal boundary $(\tau, z_b(\tau))$. Indeed, the integration of the momentum equation in (3.2) yields that, along rays $z = z_b(\tau) + (t - \tau)u_b(\tau)$ the liquid velocity is $u = u_b(\tau)$. Moreover,
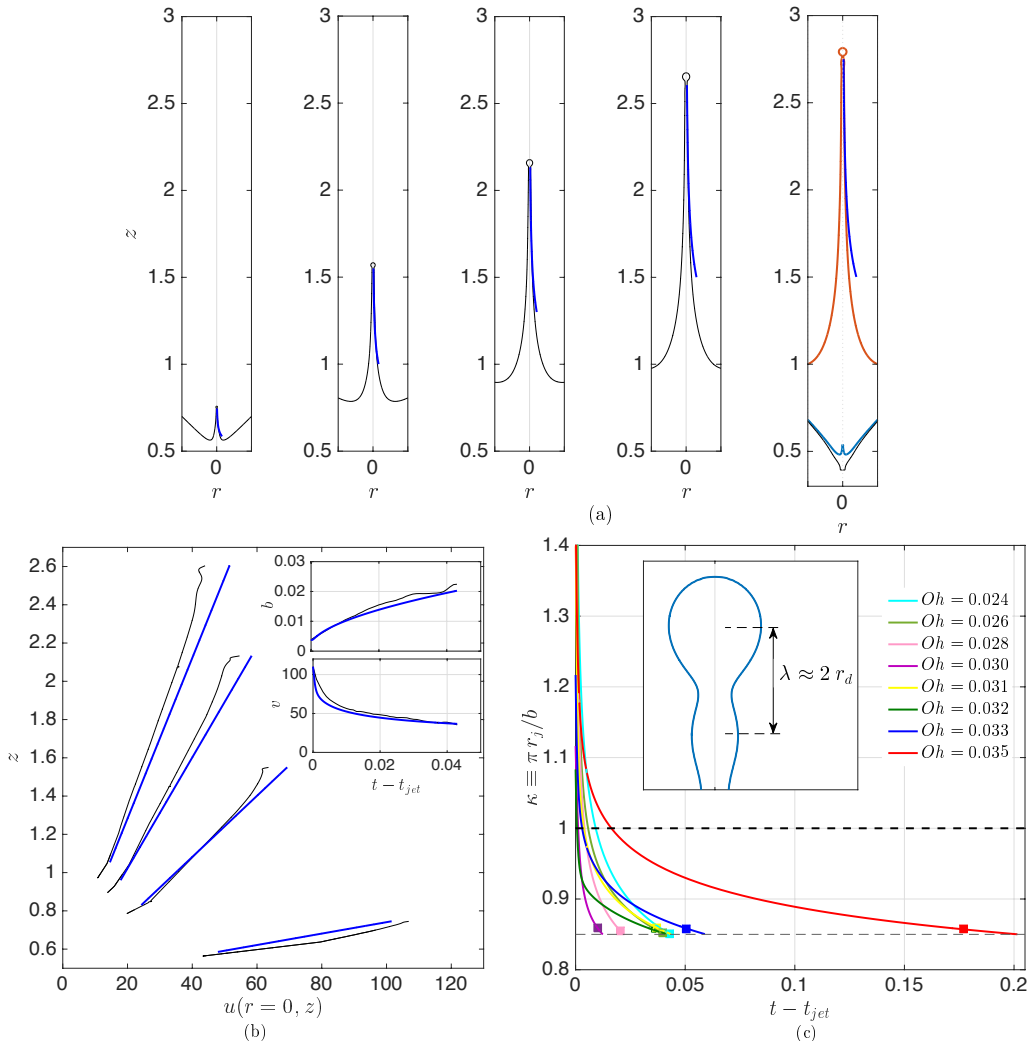
FIGURE 3. (a) Time sequence showing the comparison between the spatio-temporal evolution of the jet radius and the model prediction (blue line) calculated for $Bo = 0.01$ and $Oh = 0.024$ at the following instants of time: $t = 0.463, 0.476, 0.489$ and 0.502. The last frame in the sequence corresponds to the instant of time, $t = 0.506$, the jet breaks into drops and includes the shapes of the jet for instants of time close to its inception to stress the fact that the final drop diameter is much larger than the initial one. (b) Comparison between the spatio-temporal evolution of the jet velocity calculated numerically and that predicted by the model (blue line). The predicted values could be closer to the calculated ones if the pressure gradient term was added into the momentum equation (3.2), as it is shown in the Supplementary Material. (c) The different continuous lines indicate the time evolution of the dimensionless wavenumber calculated solving equations (3.1) using the analytical expressions in (3.7) for values of the Ohnesorge number around the one the minimum drop radius is attained. The breakup instants calculated using GERRIS, which are indicated using filled squares, reveal that a drop is ejected when the value of the ratio $\pi\, r_j/b$ calculated using the system (3.1), is such that $\pi\, r_j/b = 0.85$.

to integrate the continuity equation in (3.2) it is first convenient to notice that

$$\frac{\partial}{\partial z}\left(\frac{\partial u}{\partial t} + u\frac{\partial u}{\partial z}\right) = 0 \Rightarrow \frac{DS}{Dt} + S^2 = 0 \Rightarrow -\frac{DS}{S^2} = Dt \Rightarrow S = \frac{S_b(\tau)}{1 + (t - \tau)\, S_b(\tau)}, \quad (3.3)$$

with (see Gekle & Gordillo 2010)

$$S_b(\tau) = \frac{\partial u}{\partial z}(\tau, z_b(\tau)) = -\frac{du_b/d\tau}{u_b(\tau) - dz_b/d\tau}. \tag{3.4}$$

Therefore, the substitution of equation (3.4) into the continuity equation in (3.2) yields

$$\frac{D}{Dt}\left(\ln r^2\right) = -\frac{S_b(\tau)}{1 + (t - \tau)S_b(\tau)} \Rightarrow r = \frac{r_b(\tau)}{\sqrt{1 + (t - \tau)S_b(\tau)}}. \tag{3.5}$$

The inertio–capillary balance existing for values of the Ohnesorge number $Oh \sim Oh_c$ (Gordillo & Rodríguez-Rodríguez 2019) during a short interval of time after the jet is ejected causes the time evolution of the jet to be self–similar (Zeff *et al.* 2000; Brasz *et al.* 2018; Lai *et al.* 2018), a fact yielding that the liquid velocity and the jet radius at $z_b(\tau)$ can be respectively expressed as $u_b(\tau) = u_0\,\tau^{-1/3}$ and $r_b(\tau) = r_0\,\tau^{2/3}$. Defining the origin of the jet region at the vertical position $z_b(\tau) = u_0\,\tau^{2/3}$, making use of equation (3.4) and of the fact that $u_b(\tau) = u_0\,\tau^{-1/3}$ and that $z = z_b(\tau) + u_b(\tau)(t - \tau)$, yields

$$S_b(\tau) = 1/\tau \quad \text{and} \quad \tau = (u_0\,t/z)^3. \tag{3.6}$$

The substitution of equations (3.6) into $u = u_0\,\tau^{-1/3}$ and into equation (3.5) yields

$$u(z,t) = \frac{z + z_0}{t + t_0}, \quad r(z,t) = \delta\frac{(t + t_0)^3}{(z + z_0)^{7/2}}, \tag{3.7}$$

with $\delta = r_0 u_0^{7/2}$ and where t_0 and z_0 account for the fact that both the time and the vertical position in the ballistic equations are shifted with respect to the respective origins in the numerical simulations. The values of t_0, z_0 and δ in equations (3.7) are determined making use of the numerical values of v_j, r_j and of the strain rate, S, calculated from the numerical simulations right after the jet is ejected, [see figure 1]. The parameter δ, which measures the ratio between inertial and interfacial tension forces always satisfies the condition $\delta \gg 1$, this being the reason why the capillary pressure gradient could be neglected in the momentum equation (3.2) (see the Supplementary Material for details of the solution including the capillary pressure gradient term). Indeed, in spite of its simplicity, the model expressed by equations (3.1), solved using the analytical expressions in (3.7), correctly reproduces the time evolutions of the radius and vertical liquid velocity within the jet, $r(z,t)$ and $u(z,t)$, in a finite spatial region located upstream the drop, which suffices to correctly evaluate the mass and momentum fluxes entering the drop, see figures 3(a)-(b). Let us point out that the very good agreement depicted in figures 3(a)-(b) between the jet shapes calculated numerically using GERRIS and our analytical prediction in (3.7), could have been extended to a larger spatial region. This could have been done providing correct boundary conditions to the parabolic set of equations (3.2) during a longer time period. However, it is not our goal here to predict the full shapes of the Worthington jets, but the diameters and the velocities of the droplets ejected. In this regard, the insets in figure 3(b) show that the time evolutions of the radius and the velocity of the tip of the jet predicted solving equations (3.1) and (3.7) (blue lines) closely follow the time evolutions calculated numerically using GERRIS (black lines). We checked that the good agreement shown in figure 3(a)-(b) between predictions and numerical results extends to the whole range of values of Oh investigated here.

Since the theoretical model presented here is able to correctly capture the time evolutions of both $v(t)$ and $b(t)$ (see the inset in figure 3(b)) the only missing ingredient in order to predict the drop radius and drop velocity is to determine the instant of time the jet tip breaks into drops.

3.1. *Jet breakup condition*

The radius and the velocity of the first droplet ejected is calculated here particularizing the functions $b(t)$ and $v(t)$ (see the inset in figure 3(b)) at the instant the jet tip breaks as a consequence of the growth of a capillary instability. Since the wavelength of the capillary perturbation can be approximated by the diameter of the droplet, as it is suggested by the inset of figure 3(c), our criterion for capillary breakup can be expressed as the instant of time for which the dimensionless wavenumber, $\kappa = \pi r_j(t)/b(t)$, verifies the condition $\pi r_j/b = \kappa_c$, with $\kappa_c < 1$ (Rayleigh 1878) a constant. We do not predict here the value of this free constant κ_c, but fix it here by comparing the model predictions with the numerical results. Indeed, figure 3(c) represents, with continuous lines, the time evolutions of the ratio $\pi r_j(t)/b(t)$ obtained solving the model equations (3.1) using the analytical expressions in (3.7) for several values of Oh. In each of these curves, we include a filled square corresponding to the jet breakup time calculated using GERRIS and, in all cases considered, we find that the breakup instant predicted using the GERRIS values takes place when the ratio $\pi r_j/b$ calculated using our model verifies the condition $\pi r_j/b = \kappa_c$, with $\kappa_c = 0.85$. This fact confirms our hypothesis that the breakup instant can be characterized through the value of the ratio $\pi r_j/b$. Notice that the value for κ_c found here is slightly larger than the dimensionless wavenumber of fastest growth rate of capillary perturbation calculated by Rayleigh (1878) for the case of cylindrical jets, $\kappa_c \simeq 0.7$. However, this is not surprising in our case because Gordillo & Gekle (2010) reported that the wavelengths of capillary perturbations leading to the end-pinching of stretched Worthington jets is close to the jet perimeter, which implies values of the dimensionless wavenumber of fastest growth rate larger than 0.7.

The insets in figure 4 show the comparison between the values of r_d and v_d calculated numerically using GERRIS (full symbols) and those predicted by our model (open symbols), the latter obtained solving equations (3.1) and applying the jet breakup condition $\pi r_j/b = 0.85$. The inset in figure 4(a) shows that most of the predicted values overlap the ones calculated using GERRIS. The good agreement between predictions and numerical results in the complex region where both r_d and v_d behave non monotonically with Oh, validates our approach.

3.2. *Scaling the size and velocity of the primary droplet*

While the model developed in the previous sections is capable predict, with great accuracy, the diameters and velocities of the first drop ejected, it is of little practical use since it requires to solve a system of ordinary differential equations. The purpose here is to derive approximate algebraic equations for both r_d and v_d making use of our recent result in Gordillo & Rodríguez-Rodríguez (2019), where we derived expressions for both the radius and the velocity of the incipient jet, r_{jet} and v_{jet} respectively (see figure 1a), as a function of the Ohnesorge number.

The model represented by equations (3.1) and (3.7) and, most importantly, the breakup criterion deduced here, $\pi r_j/b = 0.85$, are free of parameters, exceptuating the small air drag term in equation (3.1) -which, in fact, we could have neglected. Since the system of differential equations only receives information of the bulk flow through the initial conditions, which depend on $Oh^{1/2}$ for $Oh < Oh_c$, we assume that

$$r_d = r_{jet} + f(Oh^{1/2}) \simeq r_{jet} + C_1 + C_2\,Oh^{1/2} + O(Oh)\ , \tag{3.8}$$

where we have made use of the fact that $Oh \ll 1$. Hence, making use of equations (2.1)
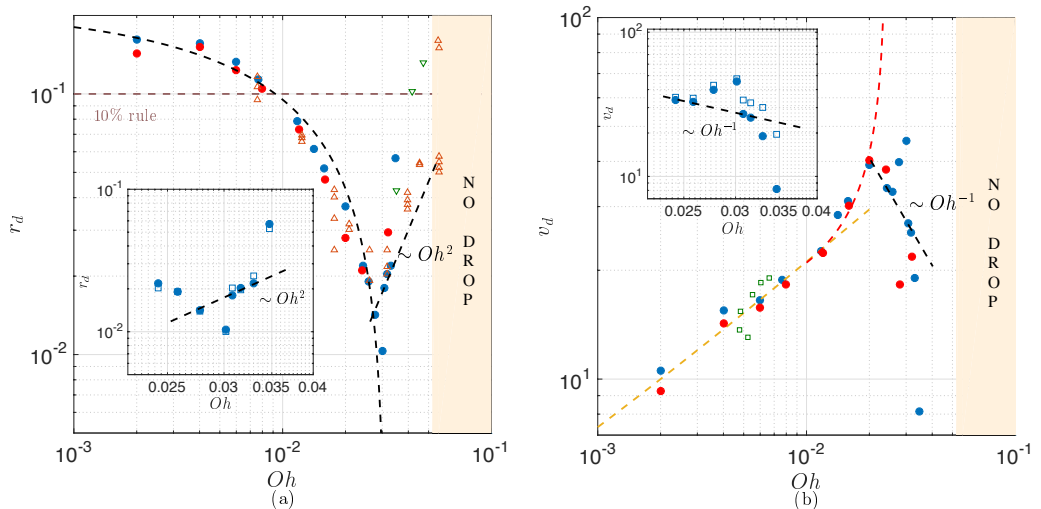
FIGURE 4. Numerical results for the radius (a) and velocity (b) of the top droplet ejected after the bursting of a bubble for $Bo = 0.01$ (solid blue dots) and $Bo = 0.05$ (solid red dots). Figure (a) includes the experimental data reported in Brasz *et al.* (2018) (orange and green triangles) as well as the predicted values of r_d calculated using either equation (3.9) or $r_d = 18.45\,Oh^2$, finding a fair agreement between the predicted and calculated values. The minimum value of r_d is reached at $Oh = 0.03$. Figure (b) includes the droplet velocities reported in Ghabache *et al.* (2014) (green squares) and the predicted values of v_d using either equation (3.10) or $v_d = 0.784\,Oh^{-1}$, finding a fair agreement between the predicted and calculated values. The insets in (a)-(b) show the predictions of the full model with $\kappa_c = 0.85$ (see figure 3 (c)) for values of the Ohnesorge number in the region where both r_d and v_d experience abrupt variations with Oh, finding a fair agreement between the values calculated using GERRIS (filled symbols) and the full model (open symbols): notice that both data sets mostly overlap.

and (3.8), the radius of the ejected droplet can be expressed as

$$r_d = K_b(Bo)\left(1 - (Oh/Oh'_c(Bo))^{1/2}\right) \quad \text{if} \quad Oh < Oh'_c, \qquad (3.9)$$

with $K_b(Bo)$ and $Oh'_c(Bo) > Oh_c(Bo)$ constants that, we found, hardly vary with Bo for $Bo \leqslant 0.05$. Following the same reasoning as before, since the initial radius of the jet scales as $r_{jet} \propto Oh^2$ when a bubble is entrapped (see equation 2.3), it is also expected that $r_d \propto Oh^2$ for larger values of the Ohnesorge number.

Figure 4(a) shows that the values of r_d calculated using (3.9) with $K_b = 0.22$, $Oh'_c = 0.031$, compare favourably with the numerically calculated ones for $Oh \lesssim 0.028$ and also that $r_d = 18.45\,Oh^2$ approximates well the data for the small interval of values $0.028 \leqslant Oh \leqslant 0.035$. We found, however, no simple way of predicting r_d in a very short range of values around $Oh = 0.03$ and also around $Oh \approx 0.04$, but the complex dependence close to these two values of Oh is reproduced by the full model, which requires the integration of ordinary differential equations, as it is shown in the inset of figure 4(a). Our numerical results in figure 4(a) also reveal that no droplets are ejected for $Oh \gtrsim 0.04$. Indeed, the $r_d \propto Oh^2$ prediction deteriorates for the larger values of Oh because, for values of the Ohnesorge number $Oh \approx Oh_d$, the amplitude of the capillary waves excited during the rim retraction process are highly attenuated by viscosity, reducing the size of the entrapped bubble or even preventing the entrapment (see figure 2) and, as a consequence, reducing the intensity of the Worthington jet.

Let us finally point out that the numerical results depicted in figure 4(a) also show that
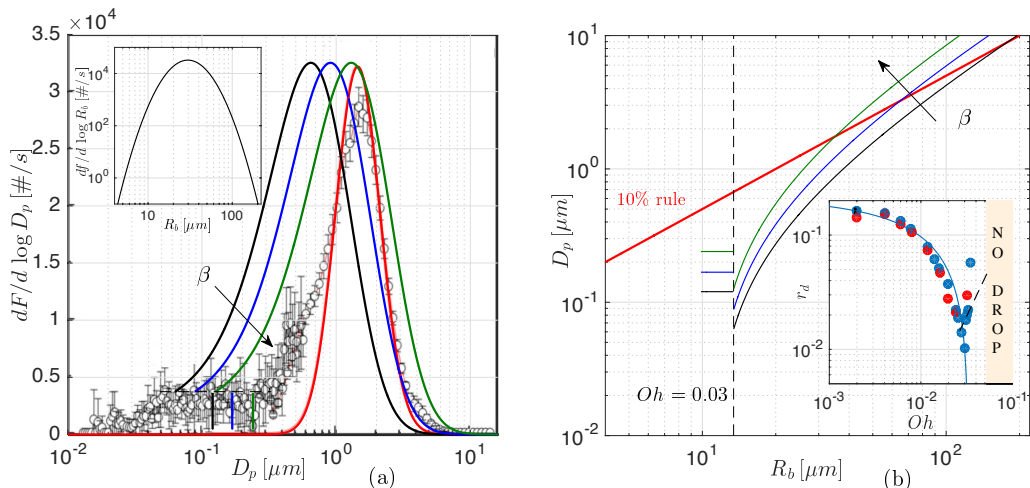
FIGURE 5. (a) (Adapted from figure 1 in Wang *et al.* (2017)): Comparison between the predicted and measured particle diameters composing the aerosol with $D_p = \beta R_b r_d$ and $\beta = 0.5$ (black), 0.7 (blue) and 1 (green), see also figure (b). The inset represents a log-normal fit to the experimental data in Wang *et al.* (2017). (b) Particle diameters calculated as $D_p = \beta R_b r_d$ with r_d given in equation (3.11). Seawater physical properties taken from Nayar *et al.* (2016) for a temperature of 25° C and a salinity of 30 g/kg. Here # indicates number of particles or bubbles and f or F indicate the bubble or particle size distribution.

the main influence of the Bond number on r_d is appreciated at the minimum radius, with $min(r_d(Bo = 0.05)) \simeq 0.015$ and $min(r_d(Bo = 0.01)) \simeq 0.01$.

Following the same reasoning as before, the velocity of the droplets ejected can also be expressed, for $Oh < Oh_c$, as $v_d = v_{jet} + g(Oh^{1/2}) \simeq v_{jet} + D_1 + D_2\,Oh^{1/2}$ with v_{jet} given in equation (2.2) and hence, figure 4(b) represents the functions

$$v_d = 1 + 31\,(Oh/Oh_c)^{1/2} \quad \text{if} \quad Oh < 0.01,$$
$$v_d = 12.5\left(1 - (Oh/Oh_c)^{1/2}\right)^{-1/2} \quad \text{for} \quad 0.01 \leqslant Oh < 0.024 \quad \text{and} \tag{3.10}$$
$$v_d = 0.784Oh^{-1} \quad \text{for} \quad Oh > 0.024\,,$$

with the latter expression for v_d in (3.10) motivated by equation (2.3). Once the free constants are properly chosen, the function $v_d(Oh)$ in equation (3.10) agrees well with the numerical results depicted in figure 4(b) except when Oh approximates either Oh_c or Oh_d, for the reasons explained above. In these cases, the full model should be used to predict v_d, as the inset of figure 4 (b) shows. To further test the utility of our simplified description presented here, which already predicts the trend exhibited by the experimental data reported in Brasz *et al.* (2018) (see figure 4(a)), we have made use of the results in Wang *et al.* (2017) who, in their figure 1, provided the measured aerosol particle flux produced by a flux of bubbles with a certain size distribution (see figure 5(a)). Assuming that each bubble produces just one drop, using the 10% rule for r_d and approximating the dry diameter as $D_p = 0.5\,R_d$, Wang *et al.* (2017) obtained the red line in figure 5(a), which compares favourably with part of the experimental data, but which does not predict the production of submicrometric particles, which play an essential role in atmospheric dynamics (Wang *et al.* 2017). Figure 5(a) also includes the distribution of particles calculated assuming that just one single drop is produced per bursting bubble, taking $D_p = \beta R_d$ with β a parameter that accounts for evaporation effects and using

the equation for r_d:

$$r_d = 0.2 \left(1 - (Oh/0.033)^{1/2}\right) \quad \text{if} \quad Oh \leqslant 0.03 \quad \text{and}$$
$$r_d = 18.45 \, Oh^2 \quad \text{for} \quad 0.03 < Oh \leqslant 0.035 \tag{3.11}$$

which also approximates very well the numerical data (see the inset in figure 5(b)). In Wang *et al.* (2017) and references therein, it is assumed that $\beta = 0.5$ namely, that the radius of the solid particle is just one-half the original radius. But we have not found a clear justification for this particular value of β and have chosen to vary this parameter between $\beta = 0.5$ and $\beta = 1$, the latter value meaning that, after evaporation, the radius of the solid particle coincides with the initial drop radius.

The shape of the distribution of diameters obtained using our results is quite similar to the experimental one and, although slightly shifted to the left, it predicts the generation of submicron-sized particles with diameters $D_p < 100$ nm. In any case, the differences between the predicted and measured values can be attributed to the number of simplifying hypotheses done in the calculation of D_p: indeed, the bubble coalescence events at the interface, which would displace the original bubble size distribution to the right, are not considered here. Also, the use of equation (3.11) rests on the assumption that the collapse is axisymmetric and that the interface is not rigidized by surfactants or solid particles. While it is clear that the presence of small particles or surfactants will affect the jet ejection and breakup processes, the axisymmetry hypothesis is also easily violated under realistic conditions because collective effects and the influence of neighbouring bubbles will produce an inclined jet. This is so because geometrical asymmetries cause the capillary waves traveling along the spherical surface to not reach the bottom of the cavity at the same time, distorting the base of the truncated cone from which the jet is issued.

4. Concluding remarks

With the purpose of providing closed expressions for the radius, r_d, and velocity, v_d, of the first drops ejected from the tip of the fast and thin vertical jet produced at the base of the cavity of a bursting bubble, here we have extended the recent results in Gordillo & Rodríguez-Rodríguez (2019) by developing a one-dimensional model to describe the spatio-temporal evolution of the jet. This model, which is coupled with balances of mass and momentum at the jet tip, very well reproduces the spatio-temporal evolution of the radius of the jet, of the jet velocity field and the time variations of the thickness, $b(t)$, and velocity, $v(t)$, of the tip of the jet. The particularization of $b(t)$ and $v(t)$ at the instant of time the dimensionless wavenumber is such that capillary waves grow and break the jet, provide the values of r_d and v_d as a function of the Ohnesorge number, Oh. Since this method requires the integration of a system of equations, it is not of practical use in realistic applications. Hence, we have deduced simple algebraic equations for r_d and v_d, which are in fair agreement with our own numerical results. The equations for r_d and v_d are expressed, for $Oh \lesssim 0.03$, in terms of $Oh^{1/2}$, with $Oh^{1/2}$ proportional to the dimensionless wavelength of the capillary wave which triggers the jet ejection process from the base of a truncated cone. However, for larger values of the Ohnesorge number, the entrapment of a bubble below the jet causes viscosity to limit the maximum attainable velocity and the minimum jet radius, a fact explaining that, for $0.025 \lesssim Oh \lesssim 0.035$, the radii and velocities of the droplets ejected experience an abrupt change of trend in a narrow range of values of Oh, with the scales in this region given by $r_d \propto Oh^2$ and $v_d \propto Oh^{-1}$. The equation for r_d deduced here has been applied to predict the diameters

of the submicrometric aerosol particles produced by the bubble size distribution reported in Wang *et al.* (2017) and our results are similar to the flux of submicron-sized particles measured experimentally, a fact indicating that our findings could be used to improve the aspects of climate models related with the production of sea spray aerosol particles, which play an essential role absorbing and scattering radiation and as ice and cloud condensation nuclei.

Acknowledgements

REFERENCES

BRASZ, C. F., BARTLETT, C. T., WALLS, P. L. L., FLINN, E. G., YU, Y. E. & BIRD, J. C. 2018 Minimum size for the top jet drop from a bursting bubble. *Physical Review Fluids* **3**, 074001–.

DEIKE, L., GHABACHE, E., G., LIGER-BELAIR, DAS, A. K., POPINET, S. & SÉON, T. 2018 Dynamics of jets produced by bursting bubbles. *Physical Review Fluids* **3**, 013603–.

DUCHEMIN, L., POPINET, S., JOSSERAND, C. & ZALESKI, S. 2002 Jet formation in bubbles bursting at a free surface. *Physics of fluids* **14** (9), 3000–.

ERININ, M. A., WANG, S. D., LIU, R., TOWLE, D., LIU, X. & DUNCAN, J. H. 2019 Spray generation by a plunging breaker. *Geophysical Research Letters* **46** (14), 8244–8251.

GEKLE, S. & GORDILLO, J. M. 2010 Generation and breakup of worthington jets after cavity collapse. Part 1. Jet formation. *Journal of Fluid Mechanics* **663**, 293–330.

GHABACHE, E., ANTKOWIAK, A., JOSSERAND, C. & SÉON, T. 2014 On the physics of fizziness: How bubble bursting controls droplets ejection. *Physics of fluids* **26**, 121701–.

GORDILLO, J. M. & GEKLE, S. 2010 Generation and breakup of worthington jets after cavity collapse. Part 2. Tip breakup of stretched jets. *Journal of Fluid Mechanics* **663**, 331–346.

GORDILLO, J. M. & RODRÍGUEZ-RODRÍGUEZ, J. 2019 Capillary waves control the ejection of bubble bursting jets. *Journal of Fluid Mechanics* **867**, 557–571.

LAI, C.-Y., EGGERS, J. & DEIKE, L. 2018 Bubble bursting: Universal cavity and jet profiles. *Phys. Rev. Lett.* **121**, 144501.

DE LEEUW, G., ANDREAS, E.L., ANGUELOVA, M.D., FAIRALL, C.W., LEWIS, E.R., O'DOWD, C., SCHULZ, M. & SCHWARTZ, S.E. 2011 Production flux of sea spray aerosol. *Reviews of Geophysics* **49**, 2010RG000349.

LHUISSIER, H. & VILLERMAUX, E. 2012 Bursting bubble aerosols. *Journal of Fluid Mechanics* **696**, 5–44.

MACINTYRE, F. 1972 Flow patterns in breaking bubbles. *J. Geophysical Research* **77**, 5211–5225.

NAYAR, K.G., SHARQAWY, M.H., BANCHIK, L.D. & LIENHARD V, J.H. 2016 Thermophysical properties of seawater: A review and new correlations that include pressure dependence. *Desalination* **390**, 1 – 24.

POPINET, S. 2003 Gerris: A tree-based adaptive solver for the incompressible Euler equations in complex geometries. *Journal of Computational Physics* **190** (2), 572–600.

RAYLEIGH, LORD 1878 On the instability of jets. *Proceedings of the London Mathematical Society* **s1-10** (1), 4–13.

TAYLOR, G. I. 1959 The dynamics of thin sheets of fluid III. Desintegration of fluid sheets. *Proc. R. Soc. A* **253**, 1274.

VERON, F. 2015 Ocean spray. *Ann. Rev. Fluid Mech.* **47**, 507–538.

WANG, X., DEANE, G. B., MOORE, K. A., RYDER, O. S., STOKES, M. D., BEALL, C. M., COLLINS, D. B., SANTANDER, M. V., BURROWS, S. M., SULTANA, C. M. & PRATHER,

K. A. 2017 The role of jet and film drops in controlling the mixing state of submicron sea spray aerosol particles. *Proceedings of the National Academy of Sciences* **114** (27), 6978–6983.

ZEFF, B.W., KLEBER, B., FINEBERG, J. & LATHROP, D.P. 2000 Singularity dynamics in curvature collapse and jet eruption on a fluid surface. *Nature* **403**, 401–404.